

Experimental Study of Impact of In-Service Deterioration on Thermal Performance of High-Pressure Nozzle Guide Vanes

Mathias Michaud

Department of Engineering Science,
University of Oxford,
Parks Road,
Oxford OX1 3PJ, UK
e-mail: mathias.michaud@eng.ox.ac.uk

Nafiz H. K. Chowdhury

Department of Engineering Science,
University of Oxford,
Parks Road,
Oxford OX1 3PJ, UK
e-mail: md.chowdhury@eng.ox.ac.uk

Thomas Povey¹

Department of Engineering Science,
University of Oxford,
Parks Road,
Oxford OX1 3PJ, UK
e-mail: thomas.povey@eng.ox.ac.uk

In this paper, we analyze the impact of in-service deterioration on the overall thermal performance (metal effectiveness) of heavily cooled high-pressure nozzle guide vanes of a design typical of large civil jet engines. We study 15 deteriorated parts (increased surface roughness, thermal barrier coating spallation and sintering, damaged film cooling holes, and trailing edge burn-back) from operational engines and compare their thermal performance to that of equivalent new parts. A companion paper focuses on the aerodynamic impact of in-service deterioration. Overall cooling effectiveness measurements were performed in the Engine Component AeroThermal (ECAT) Facility at the University of Oxford, at engine-representative conditions of Mach number, Reynolds number, coolant-to-mainstream pressure ratio, and turbulence intensity. We characterize the degradation of overall cooling effectiveness with service time. This is an important result for whole-life modeling. Changes in overall cooling effectiveness were greatest on the pressure surface and early suction surface of the parts. Area-averaged differences in overall cooling effectiveness of -1.83% and -10.41% were measured on the pressure surfaces of mid-life and end-of-life vanes, respectively. In the analysis, we attempt to decouple the contributions from independent deterioration effects and compare the philosophy of this top-down approach to the bottom-up approach in which effects are studied in isolation and then superposed in modeling. [DOI: 10.1115/1.4055864]

Keywords: boundary layer development, fluid dynamics and heat transfer phenomena in compressor and turbine components of gas turbine engines, heat transfer and film cooling, turbine blade and measurement advancements, turbomachinery blading design

Introduction and Related Literature

High-pressure (HP) nozzle guide vanes (NGVs) operate in a hostile environment and deteriorate with service time due to oxidation [1], deposition of airborne and fuel contaminants [2], thermal fatigue cracking [3] (e.g., of the thermal barrier coating (TBC) layer), and erosive impact-abrasion [4]. These deterioration mechanisms cause local changes in surface roughness and global changes in geometry [5,6]. TBC spallation and cracking at the leading edge (LE) are common, and TBC sintering due to long exposure to high temperatures can cause an increase in thermal conductivity [7]. The partial or complete collapse of cooling holes (smaller effective size) is often observed, as is partial blockage or geometry change of holes due to internal or external particulate deposition [8]. Partial collapse of trailing edge (TE) slots due to overheating can cause reduced TE slot coolant flow capacity. These deterioration features can exist in isolation or, more often, in parallel to varying degrees, but with complex interactive effects. Here we must recall that the vane has both an internal-cooling and (external) film-cooling system and acts as a complex heat exchanger with both forward-pass and reverse-pass elements [9–11]. The vane must properly, therefore, be regarded as highly coupled both locally in the through-wall direction and globally at the system level of the vane. Because of this coupling, the physical changes associated with deterioration mechanisms impact the thermal performance of the vane in an extremely complex manner. For this reason, it is particularly

important to benchmark whole-life engine models with assessments of engine-run parts performed in an engine-realistic environment, in a so-called *top-down* approach. This is, of course, complementary to existing studies in the open literature related to the impact of surface roughness on external heat transfer coefficient (HTC) and on adiabatic film cooling effectiveness and the impact of in-service TBC deterioration on the vane wall thermal resistance. We review this literature now.

Impact of Surface Roughness on External Heat Transfer Coefficient. There have been a number of cascade experiments to assess the impact of surface roughness on the external HTC distribution of turbine components. The majority of these studies have used either simulated roughness (sandgrain, hemisphere, and truncated cone) [12–17] or surface finishes arising from manufacturing processes (e.g., milling, polishing, and coating) [18–21]. There is only one study—to the authors' knowledge—in which an engine-representative surface roughness distribution was simulated [22]. Bons [6] provides a comprehensive review of gas-turbine-relevant roughness literature up to 2010. So far as turbine component external HTC is concerned, the consensus is that an increase in surface roughness causes an increase in external HTC due to both earlier laminar-turbulent boundary layer transition and enhanced mixing in the turbulent boundary layer. This is, of course, unsurprising. Most studies [14–16,18,19,21,22] suggest that increased roughness does not significantly impact heat transfer in the laminar region of the boundary layer.

Erickson et al. [22] performed a study similar to the present one in terms of operating conditions, roughness type, roughness modeling, roughness height, and roughness distribution around the airfoil (see Ref. [23]). Using a low-speed linear cascade, the authors

¹Corresponding author.

Contributed by the Heat Transfer Division of ASME for publication in the JOURNAL OF TURBOMACHINERY. Manuscript received January 31, 2022; final manuscript received August 15, 2022; published online November 7, 2022. Assoc. Editor: Giovanna Barigozzi.

measured the external heat transfer distribution on two vanes: a *reference* vane which has an aerodynamically smooth (roughness height not reported) surface and a *rough* vane which has the entire pressure surface (PS) and the first 10% of the suction surface (SS) roughened with a surface profile generated by an accelerated deposition facility to simulate in-service roughening, and with the remaining SS of the same surface finish as the reference case. The normalized (by tangential chord C) equivalent sandgrain roughness height (k_s) of the roughened surface was $k_s/C = 0.98 \times 10^{-3}$. Measurements were taken over an exit Re (based on the tangential chord) range $0.50 \times 10^6 < \text{Re} < 2.0 \times 10^6$ and Tu range $0.70\% < \text{Tu} < 13.5\%$. In agreement with other literature, they measured increased HTC on the vane, and attributed this to both earlier laminar-turbulent boundary layer transition and enhanced mixing in the turbulent boundary layer. At $\text{Re} = 1.00 \times 10^6$ and $\text{Tu} = 13.5\%$, they measured area-average increases in HTC (with respect to the reference vane) up to approximately 25% and 35% on the PS and early SS, respectively. No significant change in HTC was observed on the late SS. They additionally found that the boundary layer transition onset was independent of the turbulence level and that the heat transfer in the laminar boundary layer was unaffected by roughness.

Impact of Surface Roughness on Adiabatic Film Cooling Effectiveness. We now review the literature on the impact of surface roughness on adiabatic film cooling effectiveness, η_f . Experiments have been performed using flat plates [24–28] and linear cascades [17,29]. The general trend reported is that an increase in surface roughness upstream of a film cooling row leads to a thicker boundary layer and hence a higher *effective local* blowing ratio B (or, by the same token, momentum flux ratio I) which increases the tendency for film liftoff (separation). Increased surface roughness downstream of a film cooling row was found to reduce η_f at low B due to enhanced near-wall roughness-induced turbulent mixing between coolant and mainstream flows. At high B , increased surface roughness downstream of a film cooling row was less detrimental to film cooling performance, and in certain cases increased η_f . This was thought to be the result of enhanced early mixing reducing the penetration of the jet into the mainstream. We now review the most relevant study in more detail.

Rutledge et al. [17] investigated the impact of surface roughness on adiabatic film cooling effectiveness and external HTC on the SS of a vane in a low-speed linear cascade. The exit Re (based on tangential chord) was 1.06×10^6 , the inlet Tu was 21%, and the blowing ratio range was $0.3 < B < 1.4$. The SS was cooled with a cooling row with cylindrical holes and located at a normalized surface distance $l/C = 0.208$. Two types of surfaces were considered in the study: an *aerodynamically smooth* surface (roughness height not reported) and a *rough* surface which consisted of a simulated array of cones with $k_s/C = 0.842 \times 10^{-3}$. Four surface roughness configurations were studied: a *smooth* configuration in which the entire airfoil was aerodynamically smooth; an *upstream rough* configuration with a rough surface upstream of the film cooling row; a *downstream rough* configuration with a rough surface downstream of the film cooling row; and an *all rough* configuration with a rough surface upstream and downstream of the film cooling row. For $B = 0.3$, they reported decreases (with respect to smooth configuration) in area-average adiabatic film cooling effectiveness ($\bar{\eta}_f$) of 29%, 25%, and 31% for the upstream, downstream, and all rough configurations, respectively. In contrast, for $B = 1.4$, they reported increases in $\bar{\eta}_f$ of 11%, 73%, and 86% for the upstream, downstream, and all rough configurations, respectively. The effect of roughness on $\bar{\eta}_f$ was found to be minimal for $B = 0.85$. This contrary behavior was explained by roughness-induced mixing in the case of films already attached ($B = 0.3$), and a roughness-induced decreased tendency to detach at a higher blowing ratio ($B = 1.4$). At the intermediate condition ($B = 0.85$), it might be assumed that the two effects are opposite in direction but similar in magnitude. They also reported that roughness caused an increase in external

surface heat flux (driven by changes in both η_f and HTC) of 30–70% under their operating conditions.

Impact of In-Service Thermal Barrier Coating Deterioration on Wall Thermal Resistance. We now consider the in-service deterioration of TBC and its impact on heat transfer in turbine components. There are three primary deterioration mechanisms of TBC prior to mechanical failure (i.e., spallation): sintering [30]; erosion [7,31]; and local impact damage [7,31]. We now briefly review these mechanisms. The type of TBC considered is yttria-stabilized zirconia (YSZ) produced by electron-beam physical vapor deposition (EBPVD). This is the TBC type used on the vanes in the current study.

Rätzer-Scheibe and Schulz [30] studied the effect of sintering on the thermal conductivity of EBPVD YSZ TBC. They exposed a 280 μm thick coating to air at a temperature of 1100 °C (engine-representative surface temperature) for 100 and 200 h. They found that this temperature exposure had raised the thermal conductivity of the TBC (κ_{TBC}) from $\kappa_{\text{TBC}} = 1.34 \text{ W m}^{-1} \text{ K}^{-1}$ (new) to $\kappa_{\text{TBC}} = 2.01 \text{ W m}^{-1} \text{ K}^{-1}$ after 100 h (measured at 30 °C, i.e., representative of lab conditions), an increase of approximately 50%. There was no significant change in κ_{TBC} between 100 and 200 h.

Wellman and Nicholls [31] and Darolia [7] reviewed the literature (to 2007 and to 2013, respectively) related to erosion (mechanical-abrasive removal) and impact damage (compression damage) of TBC, including EBPVD TBC. Wellman and Nicholls [31] and Darolia [7] reported that TBC can be significantly eroded by ingested particles during engine operation. Erosion rates were greater at the LE and on the SS than on the PS. They also reported that the impact of particles under a high temperature can compact the TBC. Erosion and impact damage during service, therefore, act to reduce the thermal resistance of the TBC by reducing its thickness. The results vary widely with service environment and duration—with erosion between 0% and 100% of original coating thickness—and therefore it is hard to draw generalized quantitative conclusions.

Objective of This Study. Current understanding of the impact of deterioration on the thermal performance of turbine components is based on a series of simplified studies in which individual deterioration features are isolated, modeled, and tested. In this bottom-up approach (see discussion in Ref. [32]), it is necessary to build a model in which individual effects are superposed. This approach introduces error in the superposition (reliance on many individual correlations) and does not allow for the possibility of coupling. An alternative approach is the top-down approach, in which a statistically relevant set of real-engine parts subject to in-service deterioration are directly characterized by engine conditions. This approach has the advantage of providing a direct assessment of the change in performance, suitable—for example—for building whole-life engine models, but the disadvantage is that it is relatively difficult to de-couple individual effects. In this study, we take the latter approach and characterize—in detail—the change in overall cooling effectiveness (so-called *metal effectiveness*) with in-service deterioration. We do this using a set of 15 engine-run parts and two new parts, in a test at engine-representative conditions of exit Mach number, Reynolds number, and coolant-to-mainstream pressure ratio. We use supplementary testing (e.g., coolant capacity measurements) and modeling to provide insight into the driving mechanisms for the observed changes in performance.

Characterization of Test Components

We now characterize the vanes that were used for this study. Two sets of real-engine in-service-deteriorated vanes from modern large civil jet engines were used. Set 1 was composed of 12 mid-life parts

Table 1 Descriptive summary of the operation history of the in-service-deteriorated parts, and corresponding reference parts, in set 1 and set 2

Parameter	Set 1	Set 2
Number of vanes	12 (+1 new)	3 (+1 new)
Position in life cycle	Mid-life	End-of-life
Operating environment	Non-sandy	Non-sandy

and one reference part. Set 2 consisted of three end-of-life parts and one reference part. The vanes in set 1 and set 2 are from the same engine class, but had slightly different as-new geometries: comparison between sets should therefore be avoided. All the vanes are fully featured, including film cooling holes, TE slots, and TBCs. The deteriorated vanes in a particular set were from the same engine, and therefore had been operated in the same environment and have the same number of cycles. A summary of the operation history of both sets of vanes is given in Table 1. Individual vanes are identified using their set number (S1 or S2) and vane number within the set (V1, V2, etc.). Experimental data were acquired for all the vanes within set 1 and set 2. In this paper, we present detailed measurements for only four vanes within each set (one new vane and three deteriorated vanes), but high-level statistical data for the entire set. We refer to selected set 1 vane as S1-V1 (new); and S1-V2, S1-V3, and S1-V4 (mid-life). The corresponding nomenclature for set 2 is S2-V1 (new); and S2-V2, S2-V3, and S2-V4 (end-of-life). In set 1, we chose the deteriorated vanes that were the most representative of the set.

We now characterize the deterioration features of the tested vanes. We consider the changes in geometry, surface roughness, and coolant capacity. A more detailed description of the same data is presented in a companion paper [23] which deals with the characterization of the aerodynamic performance of the vanes.

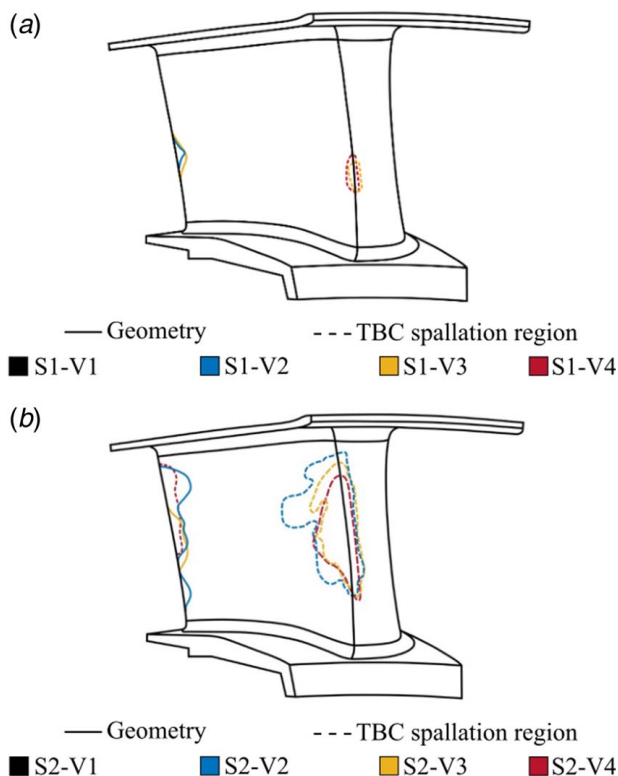


Fig. 1 Characterization of deterioration features for a selection of vanes: (a) mid-life vanes and (b) end-of-life vanes

Thermal Barrier Coating Spallation and Trailing Edge Burn-Back. We now summarize the geometry changes with deterioration. Figure 1 shows a schematic of the geometry of set 1 (mid-life) vanes S1-V1 to S1-V4 and set 2 (end-of-life) vanes S2-V1 to S2-V4. Film cooling holes and the TE slot are omitted for clarity. The solid black lines show the undamaged vanes. Colored solid and dashed lines demarcate regions of TE burn-back and TBC spallation, respectively, with individual colors for particular vanes (V2, V3, etc.) within a set. If a colored line (solid or dashed) is not shown, this means that the geometry of the deteriorated vane does not deviate from the geometry of a new vane.

First, consider the deteriorated vanes of set 1 (mid-life vanes). The mid-life vanes have only minor geometry changes. There are some very narrow (in the streamwise direction) bands of TBC spallation (exposed metal) at the LE of some vanes, covering less than 10% of the span of the vanes (see Fig. 1(a)). Most of the mid-life vanes had suffered partial collapse of the TE slot due to overheating and thermal distortion. Some vanes had notch-like TE burn-back, with notches extending to 18% of the span of the vane and to a depth of 5% of the tangential chord (see Fig. 1(a)). Film cooling holes were partially blocked due to particle deposition (see Ref. [23]), but internal cooling passages were essentially the same as new parts.

Set 2 (end-of-life) vanes exhibited more significant geometry changes. The LE of these vanes was severely damaged, with regions of TBC spallation (exposed metal) extending up to 65% of the span and 30% of the tangential chord (see Fig. 1(b)). In the showerhead region, there was significant collapse (reduction in diameter) of the film cooling holes and enchain cracking between holes (see [23]). The TE of the end-of-life vanes had severe TE burn-back, with the damage extending across 80% of the span and to a depth of 14.2% of the tangential chord. The film cooling holes were also partially blocked due to particle deposition. Despite the relatively severe external damage, the internal cooling passages were essentially the same as the new parts.

Coolant Capacity. We now summarize the change in coolant capacity due to in-service deterioration. Coolant capacity is defined

$$\Gamma_c = \frac{\dot{m}_c \sqrt{T_{0c}}}{p_{0c}} \quad (1)$$

where \dot{m}_c is the total coolant mass flowrate, and p_{0c} and T_{0c} are the total pressure and total temperature of the coolant flow in the feed plenum (see Fig. 2(a)). Measurements of coolant capacity were performed ex-situ (i.e., in the absence of the potential field developed by the vane) on individual vanes in a bench-test experiment (EXP) to separate effects on a per-vane basis. Measurements were taken with all film cooling holes and the TE slot open, and also with the TE slot sealed but films open. This allowed the separation of the film coolant capacity and the TE slot coolant capacity. By using a low-order model which takes the in situ aerodynamic fields as one of its inputs, it is possible to infer the in-situ coolant capacity from the ex-situ measurements. The process is explained in more detail in Ref. [23].

Taking all 12 deteriorated vanes within set 1 (mid-life), the mean proportional changes in coolant capacity with respect to the reference vane were -2.20% for the film holes and -4.87% for the TE slot. The changes appeared to be primarily associated with particle deposition (blockage) within the film holes, and partial collapse of the TE slot due to overheating. Photographs of these effects are shown in Ref. [23].

Taking the three deteriorated vanes of set 2 (end-of-life) the mean proportional changes in coolant capacity with respect to the reference vane were -5.77% for the film holes and -16.8% for the TE slot. For the end-of-life vanes, the decreased coolant capacity appears to be primarily associated with the collapse of the film cooling holes in the region of spalled TBC (local overheating), an effect that is partially offset by weeping cracks in the same region. The decrease in TE slot coolant capacity was caused by

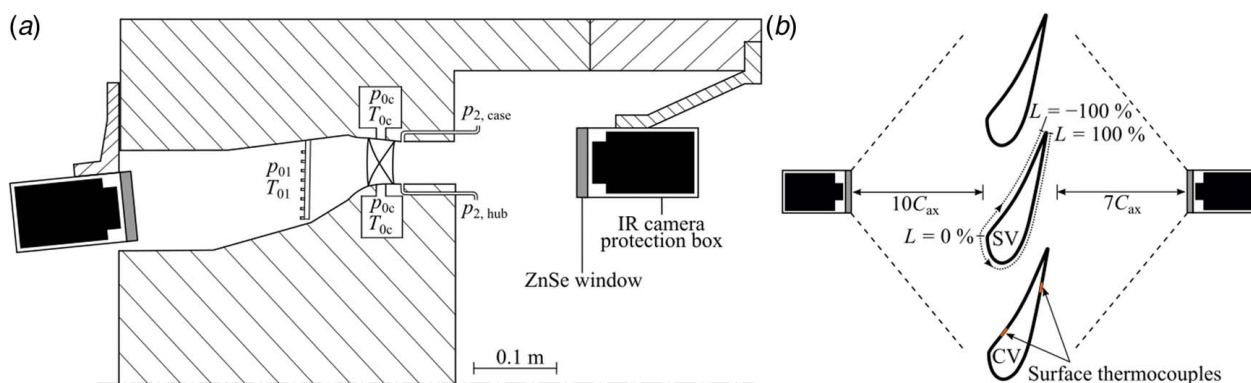


Fig. 2 (a) Schematic cross-section of the ECAT facility working section showing infrared camera locations and (b) two-dimensional unwrapped schematic of the cascade

the same mechanism as for mid-life vanes (partial collapse associated with overheating) but the severity and radial extent of damage were significantly greater.

Changes in coolant capacity for individual vanes are presented and analyzed in the companion paper [23].

Surface Roughness Measurements. In this section, we summarize changes in surface roughness with in-service deterioration. Profilometry measurements were performed using an Alicona InfiniteFocus profilometer (noncontact optical three-dimensional surface measurement system) at 21 locations on each vane surface. Measurements were taken at three span fractions (20%, 50%, and 80% span) and three relatively equidistant streamwise positions on the PS, and four relatively equidistant streamwise positions on the SS (exact measurement positions presented in Ref. [23]). Profilometry data was used (at each location) to calculate the equivalent sandgrain roughness height, k_s , using the methodology proposed by Bons [33]. Results are normalized by the tangential chord, C , of the vanes. In-service roughening was found to be most significant on the PS and early SS of the vanes and was primarily attributed to particle deposition rather than oxidation. The late SS was found to be only slightly rougher for deteriorated parts than the new TBC. Table 2 summarizes the mean values of k_s/C measured on the PS and early SS (12 measurement regions), and on the late SS (9 measurement regions). More details of the measurement method, roughness modeling, and spatial distribution of k_s/C on individual vanes can be found in Ref. [23].

Experimental Facility and Measurement Techniques

Overall cooling effectiveness measurements were conducted in the Engine Component AeroThermal (ECAT) Facility at the University of Oxford [32]. This is a high technology readiness level (TRL) blowdown facility capable of testing an annular cascade of HP NGVs at engine-representative conditions of Mach number, Reynolds number, and coolant-to-mainstream total

pressure ratio. Much of the research in the facility is focused on vanes from operating engines. Figure 2(a) shows a schematic cross-section of the facility working section with the infrared (IR) cameras installed and Fig. 2(b) shows an unwrapped schematic of the cascade. In this campaign, the overall cooling effectiveness was measured on the PS and early SS of the vanes by the upstream IR camera, and on the late SS of the vanes by the downstream camera.

Facility Operation and Test Conditions. During a test, high-pressure air stored in large (60 m³) tanks is discharged through the cascade (Table 3). For overall cooling effectiveness measurements, the facility is operated in regulated blowdown mode, with a constant inlet supply pressure allowing quasi-steady conditions for approximately 60 s. The time constant of the part is approximately 3 s, and therefore quasi-steady-state is achieved in a small fraction of the overall run time. The mainstream air is heated using two 1 MW air heaters, which increase the mainstream temperature by approximately 50 K above ambient. Coolant air is drawn from the same system, feeding independent hub and case manifolds (see Fig. 2(a)). The facility operating conditions are summarized in Ref. [32]. For this particular campaign, measurements were taken at a coolant-to-mainstream total pressure ratio $p_{0c}/p_{01} = 1.027$ (engine-representative value) and at a mainstream-to-coolant temperature ratio of $T_{01}/T_{0c} = 1.20$ (below engine-representative). The conditions overall can be taken to be highly engine-representative, but with a mismatch in a number of non-dimensional parameters of secondary importance. Though not the primary subject of this paper, the expected offset arising from temperature ratio effects in the absolute values of metal effectiveness between ECAT facility conditions and engine conditions is expected to be approximately -0.03 (subject of forthcoming publications), with a negligible offset in the *differences* between individual tested components (primary subject of this paper). Similarly, the offset in metal effectiveness between facility and engine conditions due to mismatched Biot number is expected to be 0.01 (see calculation in Ref. [10]).

Table 2 Normalized equivalent sandgrain roughness measurements for set 1 and set 2 parts

Vane	k_s/C ($\times 10^{-6}$)	
	PS & early SS	Late SS
Reference vane S1–V1	109	107
Mean S1–V(2–13)	590	164
Mean change S1–V(2–13)	441%	53%
Reference vane S2–V1	111	109
Mean S2–V(2–4)	226	163
Mean change S2–V(2–4)	104%	50%

Table 3 ECAT facility operating conditions for the current study

Parameter	Value
Mainstream inlet total temperature, T_{01}	350 K
Mainstream inlet total pressure, p_{01}	1.90 bar
Mean vane pressure ratio, p_2/p_{01}	0.58
Mean vane isentropic exit Mach, $M_{2, \text{is}}$	0.92
Vane exit Reynolds number, Re_C	1.60×10^6
Vane inlet turbulence intensity, Tu	12%
Operating temperature ratio, T_{01}/T_{0c}	1.20
Operating pressure ratios, p_{0c}/p_{01}	1.027
Coolant mass fractions, \dot{m}_c/\dot{m}	10%

Instrumentation for Overall Cooling Effectiveness Measurements. Mainstream total pressure and total temperature measurements upstream of the cascade (p_{01} and T_{01}) were performed using probe rakes (approximate axial location shown in Fig. 2(a)).

Hub and case coolant cavity total pressure and total temperature (p_{0c} and T_{0c}) were measured at four circumferential positions. The vane exit static pressure ($p_{2,hub}$ and $p_{2,case}$) was measured on six vanes (from a total of 40), with tapings located on the hub and case platform overhangs approximately 5 mm downstream of the cascade TE plane. Each of the six vanes was instrumented with six tapings at the hub and eight at the case (i.e., 84 tapings in total).

The external surface temperature of the vanes was measured using two IR cameras (FLIR A655sc) which are located within the main pressure vessel (see Fig. 2(a)), as shown in Fig. 2(b). One camera is located ten axial chords upstream of vane LE and views the entire PS and early SS of three vanes. A second camera is located seven axial chords downstream of the vane annulus and is able to view the late SS of three vanes. The cameras are installed within protective housings, sealed from the high-pressure working gas, but connected to the atmosphere via a vent line. The housings have zinc selenide (ZnSe) windows with anti-reflective coatings. The cameras can be rotated to any circumferential position in the annulus, allowing the entire vane ring to be studied.

To allow in-situ calibration of the IR measurement chain, we use a bespoke calibration system placed in the field of view (FOV) of each IR camera and assembled on to the NGV surface. The system consists of a 4 mm diameter disk of copper (approximately 0.5 mm thick) mounted over polyimide film (low thermal conductivity). The copper disk has an underside surface thermocouple (TC). This provides a region of uniform temperature, installed so as not to disturb the flow, and with low measurement error even in regions of significant through-wall and/or lateral temperature gradient (e.g., real-engine vanes). A detailed assessment of the system is provided in Ref. [34]. As shown in Fig. 2(b), two surface thermocouples are installed on a *calibration vane* (CV) adjacent to the *studied vane* (SV). This is to avoid any surface disruption on the studied vane. The surface thermocouples are installed on the early PS and late SS of the calibration vane, in the fields of view of the IR cameras.

Infrared Thermography. We now consider the details regarding IR thermography. With reference to Fig. 3 and based on the work of Kirolos and Povey [35], the IR cameras record at each pixel in their FOV the total incoming radiance, q_{cam} . This is the sum of three terms

$$q_{cam} = q'_w + q''_s + q_{opt} \quad (2)$$

where q'_w is the radiance emitted from the vane external surface

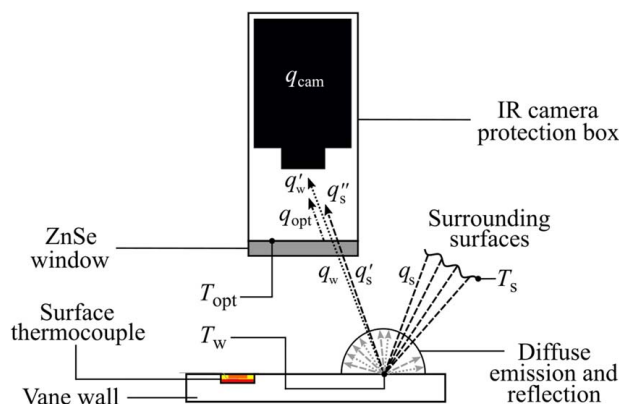


Fig. 3 Schematic of the in-situ radiation calibration system

transmitted through the ZnSe window, q''_s is the radiance emitted from the surrounding surfaces (e.g., the internal surfaces of the working section) reflected from the vane external surface and transmitted through the ZnSe window, and q_{opt} is the radiance emitted from the ZnSe window. Equation (2) can be written as

$$\sigma T_{bb}^4 = \sigma \tau_{opt} \epsilon_w T_w^4 + \sigma \tau_{opt} (1 - \epsilon_w) T_s^4 + \sigma (1 - \tau_{opt}) T_{opt}^4 \quad (3)$$

where T_{bb} is the equivalent black-body temperature recorded by the camera (obtained from a traceable black-body calibration process), σ is the Stefan-Boltzmann constant, τ is the transmissivity of the ZnSe window, ϵ_w is the emissivity of the vane external surface, T_w is the temperature of the vane external surface, T_s is the effective temperature of the surrounding surfaces and T_{opt} is the temperature of the ZnSe window. We can cast Eq. (3) as

$$q_{cam} = q'_w + q^* \quad (4)$$

where $q^* = q''_s + q_{opt}$ is called the *total surrounding radiance*.

The surface thermocouple (isothermal patch method of Ref. [34], shown in Figs. 2(b) and 3) provides a location on the vane surface at which the surface temperature is known at all instants in time. Provided the emissivity of the isothermal patch is known, this allows q^* to be determined using the method proposed by Kirolos and Povey [35]. Taking the assumption that q^* is uniform across the FOV (accurate for a diffusely reflecting—Lambertian—surface with relatively uniform background temperature) we can determine (Eq. (4)) the local surface radiance, q'_w , and so the true local surface temperature, T_w .

The surface thermocouple on the calibration vanes was overpainted with a thin layer of high-emissivity matt black paint to render the system of uniform emissivity. The matt black paint has an emissivity of 0.98 [35]. On the studied vanes, four types of (unpainted) surface are encountered in this study: as-sprayed TBC; heat-exposed TBC; deteriorated TBC; and exposed metal (in the spalled TBC region). As-sprayed TBC is found on new vanes (PS and SS) and has an emissivity of 0.98 [36,37] in the spectral range of the IR cameras (7.5–14.0 μm) [38]. Heat-exposed TBC subject to sintering (high temperatures in the engine) is found on the late SS of the deteriorated vanes (viewed by downstream IR camera, see Fig. 2(b)): here the emissivity is taken to be 0.98 [39] in the spectral range of the IR cameras. Deteriorated TBC is found on the PS and early SS (viewed by upstream IR camera) of the deteriorated vanes and its emissivity was found to be 0.98 using the method described in Appendix B. The mean transmissivity of the ZnSe windows was $\tau_{opt} = 0.95$ (manufacturer data) in the spectral range of our IR cameras. These data are summarized in Table 4.

The emissivity of the exposed metal in the spalled TBC is known to be strongly affected by surface finish and oxidation level [40–42]. It can be shown that inferred metal effectiveness is a relatively strong function of emissivity, and for this reason, data reduction in the spalled region was not attempted (uncertainty too high for data to be of value). This explains regions of missing overall cooling effectiveness data for three end-of-life vanes in the region of TBC spallation.

Overall Cooling Effectiveness Measurement Process. We now consider the process by which overall cooling effectiveness

Table 4 Emissivity of surfaces and transmissivity of ZnSe window

Parameter	Value
Emissivity of matt black paint, ϵ_p	0.98
Emissivity of as-sprayed TBC, $\epsilon_{TBC,as}$	0.98
Emissivity of heat-exposed TBC, $\epsilon_{TBC,he}$	0.98
Emissivity of deteriorated TBC, $\epsilon_{TBC,det}$	0.98
Transmissivity of the ZnSe window, τ_{opt}	0.95

(so-called *metal effectiveness*) was evaluated. Overall cooling effectiveness θ_w is defined by

$$\theta_w(L, S) = \frac{c_m(L, S)T_{01} - T_w(L, S)}{c_m(L, S)T_{01} - c_c(L, S)T_{0c}} \quad (5)$$

where T_{01} and T_{0c} are the mainstream and coolant total temperatures upstream of the vanes, respectively, $T_w(L, S)$ is the vane external surface temperature map (as a function of streamwise surface length fraction, L , and span fraction, S), and $c_m(L, S)$ and $c_c(L, S)$ are the mainstream and coolant recovery ratios, respectively, defined by

$$c(L, S) = \frac{1 + r \frac{\gamma - 1}{2} M(L, S)^2}{1 + \frac{\gamma - 1}{2} M(L, S)^2} \quad (6)$$

where M is the external Mach number distribution on the vane obtained from CFD [43] and r is the recovery factor, which is a function of the Prandtl number (Pr). For a turbulent boundary layer, r is taken to be approximately equal to $Pr^{1/3}$, where Pr is calculated based on the mainstream or coolant fluid properties (see, e.g., Ref. [44]).

The literature is not in complete consensus on the best definition of θ_w , and the definition in Eq. (5) deviates slightly from other definitions in common use. We justify this form on the simple basis that—for a system with both internal and film cooling—it is the only definition that sets the theoretical range of θ_w to be between the exact limits 0 and 1. We discussed this point in Appendix D.

In our experiments, $T_w(L, S)$ is a time average over a short period (typically ten images, acquired at 50 Hz frequency) near the end of an experimental run, at a point in time when the mainstream-to-coolant temperature difference is largest (typically 60 K). The time constant of the vane (approximately 3 s) is more than an order of magnitude lower than the time constant of facility temperature rise (approximately 60 s). Thus, overall cooling effectiveness reaches steady-state conditions (defined as within 1% of settled value) at approximately 20 s after the heaters are turned on (see analysis in Ref. [32]). Further details of the facility operation and method are discussed in Ref. [32]. Examples of full-surface θ_w maps measured on HP NGVs in the ECAT facility are presented in Ref. [32]. The uncertainty analysis on θ_w is presented in Appendix C.

Experimental Results

The experimental results are now presented. We consider the streamwise distribution of overall cooling effectiveness (three span fractions); the area-average overall cooling effectiveness; and the individual contribution of particular deterioration features to the change in overall cooling effectiveness.

Overall Cooling Effectiveness Distribution. The distributions $\theta_w(L)$, at three span fractions ($S=10\%$, 50% , and 90%), are shown in Fig. 4. Data for set 1 vanes S1–V1 to S1–V4 are shown in the top row (frames a–c, respectively) and data for set 2 vanes S2–V1 to S2–V4 are shown in the bottom row (frames d–f, respectively). Here we are concerned with changes associated with deterioration, so data within a particular set of parts (set 1 or set 2) are normalized by the maximum value of $\theta_w(L, S)$ measured within that entire set ($\theta_{w,max}$): in practice the values $\theta_{w,max}$ were all close to unity and associated with overcooled platform regions of the part (not studied in this paper). The PS is the range $L < 0\%$ and the SS is the range $L > 0\%$.

Consider first the results for the PS of reference vanes S1–V1 and S2–V1. Pressure side distributions of $\theta_w(L)$ at 10%, 50%, and 90% span were broadly similar for both reference parts. At the LE ($L = 0\%$), there is a region of high external HTC (thin boundary layer) which causes a trough in θ_w . Directly downstream of the LE, θ_w

rises as the boundary layer develops as coolant is introduced from the PS showerhead. There is a trend of gradually rising θ_w in the range $0 < L < 60\%$, with local peaks in θ_w associated with additional mid-PS cooling films are introduced. The rate of increase in θ_w is moderated by mildly increasing HTC. Towards the TE, and after the last row of film cooling holes ($L < -60\%$), we observe a decrease in θ_w , due to streamwise reduction in film cooling effectiveness as the coolant mixes with the mainstream flow. Typical bias uncertainty (β) bands for absolute values θ_w are shown for reference vane S1–V1 in Fig. 4(a). The $\pm\beta$ bands (95% confidence limits) are illustrated using semitransparent shading. Further detail is provided in Appendix C.

Now consider the results for the SS ($L > 0\%$) of reference vanes S1–V1 and S2–V1. There is a steep rise in θ_w between $L = 0\%$ until $L = 15\%$. This is driven by strongly increasing film effectiveness in the showerhead region, and a reduction in HTC as the boundary layer develops. The SS shoulder ($15\% < L < 40\%$) faces normal to the line of sight of the cameras (see Fig. 2(b)) and there is a small region in which data cannot be captured. On the late SS ($L > 40\%$), we observe a decrease in θ_w due to the streamwise reduction in film cooling effectiveness. A small local peak in θ_w at $L = 75\%$ is due to the presence of the internal TE pedestal bank, which enhances the internal HTC.

Now consider the deteriorated parts of set 1 (mid-life vanes). In the early PS and early SS region ($-15\% < L < 15\%$) distributions of θ_w are similar for the deteriorated parts and the reference part, with no consistent change due to deterioration. This result is not surprising, because in this region there are a number of effects in competition. Based on the literature we might expect the following: eroded (thinner) and more conductive TBC (due to sintering) at the LE could cause an increase in θ_w ; an increase in film cooling effectiveness might be expected with increasing roughness (true for $B \geq 1.00$ and high inlet Tu ; see, e.g., Refs. [17,27]), which would increase θ_w ; and a reduction in film coolant capacity due to deposition within holes would decrease film effectiveness and so decrease θ_w . For completeness, we also note that we would expect little impact of increased surface roughness on external HTC in any laminar boundary layer region [14–16,18,19,21,22], so little impact on θ_w , but further note the debate about the existence of a laminar region for heavily cooled NGVs with high inlet turbulence, for which it is appears likely the classical laminar-then-turbulent development (applicable to smooth flat plates with low turbulence) is inapplicable. Over the rest of the PS ($L < -15\%$), there is a distinct reduction in θ_w for the mid-life vanes compared to the reference vane. This is driven by the increase in external HTC due to increased surface roughness (see, e.g., Ref. [22]) and a reduction in film and TE slot coolant capacities caused by deposition and partial collapse, respectively. The decrease in θ_w is expected to be mitigated by an increase in TBC thermal conductivity. We note the reduction in θ_w on the PS of vane S1–V3, in a region with greater-than-average decrease in film coolant capacity but average increase in surface roughness [23]. On the SS ($L > 40\%$), a similar effect is observed: a small reduction in θ_w for the mid-life vanes compared to the reference vane. Mechanisms for this are thought to be the same as for the PS changes. We note the reduction in θ_w on the late SS of vane S1–V2, in a region with greater-than-average reduction in TE slot coolant capacity [23].

Now consider the deteriorated parts of set 2 (end-of-life vanes). Looking at the early PS and early SS region ($-15\% < L < 15\%$), we see a distinct reduction in θ_w between the end-of-life vanes and the reference vane. This is in contrast to set 1 data and is thought to be due to the shrinkage and partial collapse of the film cooling holes in the showerhead region, reducing film coolant capacity (average capacity reduction of -5.77%) and causing significantly lower film effectiveness and in-hole convective heat transfer. Photographs showing these effects are shown in the companion paper [23]. On the rest of the PS ($L < -15\%$), θ_w distributions for end-of-life parts are similar in trend to the reference part, but the absolute values of θ_w are smaller. This result is similar to, but of greater magnitude than, that for the mid-life

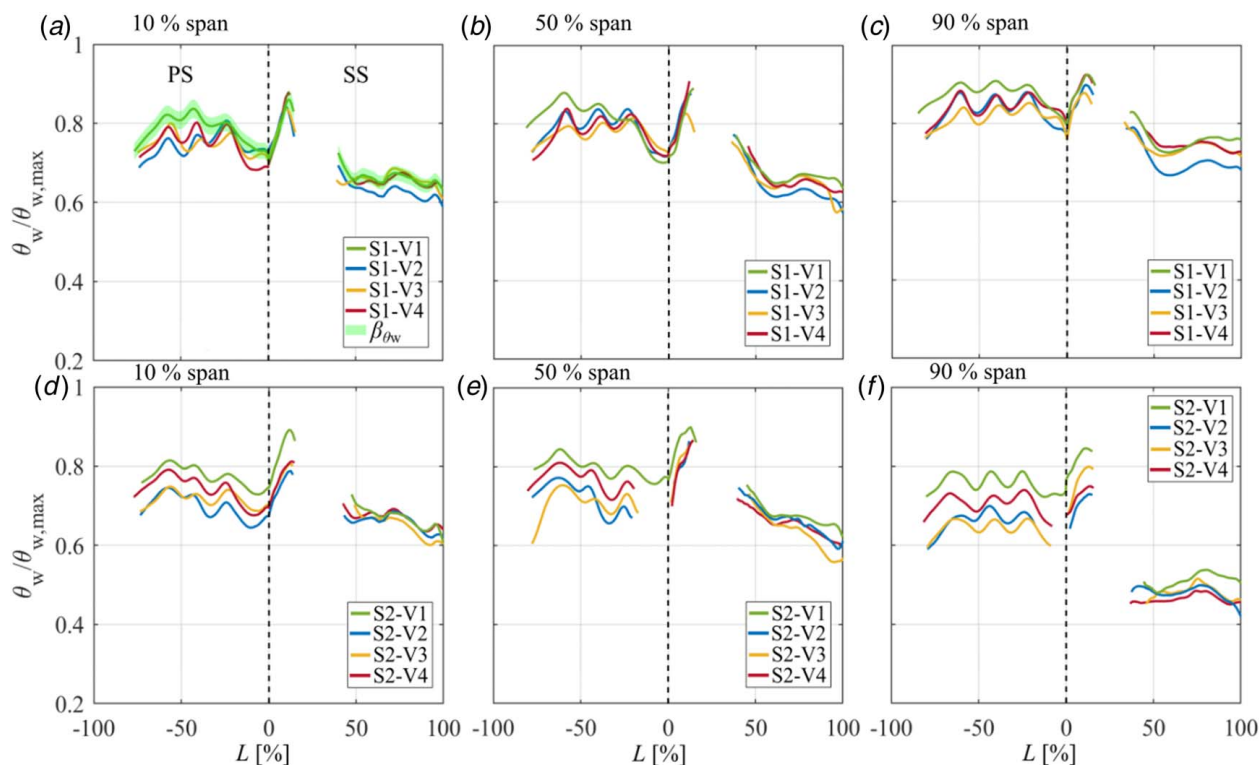


Fig. 4 Streamwise distributions of overall cooling effectiveness at 10%, 50%, and 90% span for (a)–(c) set 1 vanes and (d)–(f) set 2 vanes

parts. The mechanisms for the offset are thought to be the same. On the late SS ($L > 40\%$), the decrease in θ_w for the end-of-life vanes compared to their reference vane is similar to the corresponding result for mid-life vanes (similar increase in surface roughness on the late SS: see Table 2). The late SS film cooling holes (located just before the SS shoulder) are well outside the TBC spallation region (where film cooling holes are heavily damaged) and therefore the flow capacity of these holes would be expected to be similar to mid-life vanes: i.e., reduced only due to deposition within holes, and not due to partial collapse. We might have expected to see a greater reduction in θ_w on the late SS for end-of-life vanes compared to mid-life vanes due to a greater reduction in TE slot flow capacity (TE slot flow capacity reduction of -4.87% for mid-life vanes, and -16.8% for end-of-life vanes) causing a reduction in internal cooling mass flow in the TE circuit. This effect was not conclusively observed, however

Area-Average Overall Cooling Effectiveness. We now consider the area-average overall cooling effectiveness ($\bar{\theta}_w$) of the vanes. The normalized area-average overall cooling effectiveness $\bar{\theta}_w / \theta_{w,max}$ and the mean changes in $\bar{\theta}_w$ between the deteriorated and reference vanes are listed in Table 5. The data are separated into the following regions: PS ($-80 < L < -0\%$ for mid-life and $-80 < L < -30\%$ for end-of-life); early SS ($0 < L < 15\%$); and late SS ($40 < L < 100\%$).

Consider first the data for set 1 (mid-life). For the reference vane (S1-V1), $\bar{\theta}_w / \theta_{w,max}$ takes values of 0.80 and 0.81 on the heavily film-cooled PS and early SS, respectively, and 0.67 on the late SS. On the PS of the mid-life vanes, we observed an average reduction in $\bar{\theta}_w$ of -1.65% for the sample vanes S1-V(2–4) and -1.83% for the entire set S1-V(2–13). On the early SS, we see an increase in $\bar{\theta}_w$ of $+1.24\%$ for the sample vanes and $+1.58\%$ for the entire set. On the late SS, corresponding values are a decrease in $\bar{\theta}_w$ of -0.78% for the sample vanes and -1.32% for the entire set.

Overall, the vane-to-vane spread in the data is very low, suggesting high similarity between parts, and high similarity in the effects of degradation on the parts. Scaling the results to typical nominal engine conditions ($T_{01} = 1800$ K, $T_{0c} = 900$ K, and $\theta_w = 0.70$), the measured mean change in $\bar{\theta}_w$ for the entire set of parts (12 vanes) would correspond to changes in T_w of $+11.5$ K, -9.9 K and $+8.3$ K on the PS, early SS and late SS, respectively.

Now consider the data for set 2 (end-of-life) parts. We observe a significant decrease in $\bar{\theta}_w$ with in-service deterioration on the PS and early SS in particular. The mean changes in $\bar{\theta}_w$ for deteriorated set 2 parts (three vanes) with respect to the reference part were -10.41% , -8.53% , and -1.15% on the PS, early SS, and late SS, respectively. Scaling the results to typical engine conditions, these measured mean changes in $\bar{\theta}_w$ correspond to a change in T_w of $+65.6$ K, $+53.7$ K, and $+7.2$ K on the PS, early SS, and late SS, respectively. This is entirely in-line with the acceleration effect.

Decoupling of Effects of Individual Deterioration Features on Overall Cooling Effectiveness

In this section, we attempt to quantify the effects of particular deterioration features on overall cooling effectiveness, θ_w . For this purpose, we use a one-dimensional steady-state heat transfer model of our parts, with boundary conditions taken from open-literature data. We consider four effects: the change in external HTC caused by increased surface roughness; the change in adiabatic film cooling effectiveness caused by increased surface roughness; the change in film coolant capacity; and the change in vane wall thermal resistance due to TBC sintering. Effects such as the redistribution of coolant caused by damaged film cooling holes, cracking, TBC erosion, and increased surface roughness within film cooling holes are not explicitly modeled and are assumed in aggregate to explain the balancing change in overall cooling effectiveness between that modeled and that measured.

Table 5 Area-average overall cooling effectiveness and external wall temperature changes (with respect to reference part) for set 1 (mid-life) and set 2 (end-of-life) parts

Vane	PS	Early SS	Late SS	Vane	PS	Early SS	Late SS
	$-80 < L < 0\%$	$0 < L < 15\%$	$40 < L < 100\%$		$-80 < L < -30\%$	$0 < L < 15\%$	$40 < L < 100\%$
$\bar{\theta}_w/\theta_{w,max}$ for set 1 parts				$\bar{\theta}_w/\theta_{w,max}$ for set 2 parts			
S1-V1 (Ref.)	0.80	0.81	0.67	S2-V1 (Ref.)	0.77	0.83	0.61
S1-V2	0.80	0.82	0.65	S2-V2	0.67	0.73	0.61
S1-V3	0.78	0.81	0.68	S2-V3	0.68	0.77	0.59
S1-V4	0.79	0.83	0.67	S2-V4	0.73	0.78	0.61
Mean change S1-V(2-4)	-1.65%	+1.24%	-0.78%	Mean change S2-V(2-4)	-10.41%	-8.53%	-1.15%
Mean change S1-V(2-13)	-1.83%	+1.58%	-1.32%				
ΔT_w at nominal engine conditions ($T_{01} = 1800$ K and $T_{0c} = 900$ K) for set 1 parts				ΔT_w at nominal engine conditions ($T_{01} = 1800$ K and $T_{0c} = 900$ K) for set 2 parts			
Mean change S1-V(2-13)	+11.53 K	-9.95 K	+8.31 K	Mean change S2-V(2-4)	+65.58 K	+53.74 K	+7.24 K

The heat transfer model and the nominal boundary conditions are described in Appendix A. Two regions of the vane are modeled: the PS ($-80 < L < 0\%$) and late SS ($40 < L < 100\%$). Using representative values for all other boundary conditions, the internal heat transfer coefficient in the model is varied so that θ_w is matched to the experimental area-average value of θ_w for reference vane S1-V1, $\bar{\theta}_{w,ref}$, for the appropriate region. To study each deterioration effect, we then change a particular boundary condition from its nominal value (to represent a change due to deterioration) and calculate the resulting change in $\bar{\theta}_w$ (i.e., $\Delta\bar{\theta}_w$). The predicted changes in $\bar{\theta}_w$ arising from each deterioration effect are compared with the overall change in $\bar{\theta}_w$ due to deterioration measured between reference vane S1-V1 and the mid-life vane S1-V10. This particular mid-life vane was chosen because it has an undamaged LE and TE, and an increased surface roughness (with respect to the reference vane) similar to studies in the open literature from which typical boundary conditions for the model were taken. For vane S1-V10, average values of roughness were $k_s/C = 1.02 \times 10^{-3}$ for the PS and early SS, and $k_s/C = 0.29 \times 10^{-3}$ for the rest of the SS. The measured relative changes in $\bar{\theta}_w$ for vane S1-V10 (with respect to reference vane) were -1.47% on the PS and -1.01% on the late SS.

We now consider the predicted change in overall cooling effectiveness associated with each of the four deterioration effects (boundary condition) in turn.

Effect 1: contribution to change in external HTC (h) from increased surface roughness. Here we only consider the PS because of the scarcity of available data in the open literature relating to change in h due to (small) surface roughness changes on the late SS (as vane S1-V10). At $Re = 1.60 \times 10^6$ (interpolated) and $Tu = 13.5\%$, Erickson et al. [22] reported an increase in \bar{h} over the PS (with respect to the reference vane) of 25%. The associated predicted change in $\bar{\theta}_w$ (the result of the one-dimensional model at otherwise unchanged boundary conditions) is -7.84%. This is summarized in Table 6.

Effect 2: contribution to change in adiabatic film cooling effectiveness (η_f) from increased surface roughness. At $Re = 1.06 \times 10^6$, $Tu = 21\%$, and $B = 1.0$, Rutledge et al. [17] and Bogard et al. [29] (same experiment, data split between the two papers) reported a change in area-averaged η_f ($\bar{\eta}_f$) of +40% due to increased surface roughness upstream and downstream of cooling holes (like on the PS), and +16% due to increase surface roughness only upstream of the film cooling holes (like on the late SS). The associated changes in $\bar{\theta}_w$ are +4.44% and +1.80% on the PS and late SS, respectively.

Effect 3: contribution to change in adiabatic film cooling effectiveness of change in film coolant capacity ($\Gamma_{c,film}$). For this purpose, we use a linear model in which we assume that the change in $\Gamma_{c,film}$ corresponds to an equal change in coolant mass flowrate entering the mixing layer. It is assumed that the mass flowrate of hot gas entering the mixing layer remains the same. At the nominal operating point, an enthalpy balance shows that a 1.00% change in $\Gamma_{c,film}$ corresponds to an approximate change of 0.85% in $\bar{\eta}_f$. The change in $\Gamma_{c,film}$ for vane S1-V10 (with respect to reference vane S1-V1) is -0.31%, corresponding to a change in $\bar{\eta}_f$ of -0.26% and leading to a change in $\bar{\theta}_w$ of -0.02% and -0.02% on the PS and late SS, respectively. This effect appears to be extremely small and can be considered negligible in our particular case.

Effect 4: effect of change in TBC thermal conductivity due to sintering. Rätzer-Scheibe and Schulz [30] reported an increase from $\kappa_{TBC} = 1.34$ W m⁻¹ K⁻¹ to $\kappa_{TBC} = 2.01$ W m⁻¹ K⁻¹ after 100 h at 1100 °C for EBPVD YSZ TBC (without further increase in κ_{TBC} after 100 h of heat treatment). The associated predicted change in $\bar{\theta}_w$ is +1.04% and +1.48% on the PS and late SS, respectively. This is summarized in Table 6.

The predicted contributions from each of these four modeled deterioration effects (Table 6) are visualized in Fig. 5. The measured overall change in $\bar{\theta}_w$ and the balancing term (difference between the sum of modeled terms and measured overall change) are also shown. The balancing term can be regarded as the sum of contributions of effects not modeled. On the PS, the

Table 6 Summary of contributions from particular deterioration effects

Deterioration effect	Boundary condition change on PS	Boundary condition change on late SS	$\Delta\bar{\theta}_w$ PS	$\Delta\bar{\theta}_w$ SS
Change in \bar{h} due to increased surface roughness	$\Delta\bar{h} = +25\%$	—	-7.84%	—
Change in $\bar{\eta}_f$ due to increased surface roughness	$\Delta\bar{\eta}_f = +40\%$	$\Delta\bar{\eta}_f = +16\%$	+4.44%	+1.80%
Change in $\bar{\eta}_f$ due to reduced $\Gamma_{c,film}$	$\Delta\bar{\eta}_f = -0.26\%$	$\Delta\bar{\eta}_f = -0.26\%$	-0.02%	-0.02%
Change in κ_{TBC} due to sintering	$\Delta\kappa_{TBC} = +50\%$	$\Delta\kappa_{TBC} = +50\%$	+1.04%	+1.48%

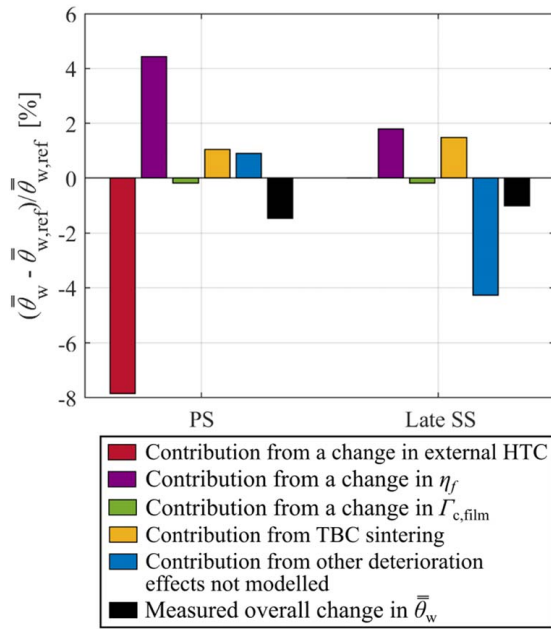


Fig. 5 Modeled and measured changes in overall cooling effectiveness, and balancing term associated with effects not modeled, including coupling effects

sum of the contributions of the modeled deterioration effects on $\bar{\theta}_w$ differs from the measured overall change in $\bar{\theta}_w$ by +0.91% (i.e., overprediction of the reduction in $\bar{\theta}_w$). This is likely to be due to an overprediction of the increase in \bar{h} due to increased surface roughness (largest term), but errors may also arise because of the inherent lack of coupling in the model.

On the SS, the sum of the contributions of the modeled deterioration effects on $\bar{\theta}_w$ differs from the measured overall change in $\bar{\theta}_w$ by -4.27% (i.e., underprediction of the reduction in $\bar{\theta}_w$). This is likely to be due to the unmodeled effect of an increase in surface roughness on the late SS (lack of available data) and the unmodeled effect of a reduction in TE slot coolant capacity (i.e., reduction in SS internal cooling).

Although this attempted decoupling goes some way to demonstrating the likely magnitude of individual uncoupled terms and gives some insight into sensitivities, the relatively poor reconciliation with measured results highlights the challenges associated with the bottom-up superposition approach, in which individual effects are studied in isolation and combined via a model. In this approach—common in turbomachinery research—errors arise for three reasons: inadequate boundary condition specification in the individual studies; lack of coupling of more complex effects; and errors or assumptions in the superposition method. In the top-down approach (style of present study, and reason for the ECAT facility, as discussed in detail [32]) the combined result can be accurately characterized, but with relatively limited insight into the driving factors. Clearly, both approaches are important for the development of understanding, but arguably the latter approach is more suited for the accurate evaluation of the aerothermal performance of turbine components.

Conclusions

In this paper, 15 in-service-deteriorated HP NGVs representing mid-life and end-of-life parts from operational engines were studied for the purpose of describing and quantifying their overall thermal performance. The deterioration features included: thermal barrier coating spallation; damaged film cooling holes; increased surface roughness; and trailing edge burn-back. The study

focused on quantifying changes in overall cooling effectiveness and on separating the effects associated with particular deterioration features.

For the mid-life vanes, the mean (12 vanes) changes in area-average overall cooling effectiveness were found to be -1.83%, +1.58%, and -1.32% on the PS, early SS, and late SS, respectively. The corresponding implied changes in metal temperature at engine conditions ($T_{01} = 1800$ K and $T_{0c} = 900$ K) are +11.53 K, -9.95 K, and +8.31 K. For the end-of-life vanes, the mean (three vanes) changes in area-averaged overall cooling effectiveness were found to be -10.41%, -8.53%, and -1.15% on the PS, early SS, and late SS. The corresponding implied changes in metal temperature at engine conditions are +65.58 K, +53.74 K, and +7.24 K. We propose these effectiveness changes and implied temperature changes at a typical engine condition as rules-of-thumb for whole-life engine modeling.

Using a simple one-dimensional heat transfer model, decoupling of contributions from particular deterioration effects was attempted. The purpose is both to get insight into particular sensitivities, but also to reflect on the philosophy of the top-down approach (present study) as compared to the more conventional bottom-up approach in which effects are studied in isolation and then superposed in modeling. We found that despite the careful choice of boundary conditions, it was difficult to reconcile the modeled effect of individual deterioration features (combined via linear superposition) with the overall change in overall cooling effectiveness measured in the experiment. Whilst some insight into the likely magnitude of individual effects was provided, confidence in the superposed result was low. This somewhat justifies the importance of top-down studies for this type of investigation.

This paper addresses an important literature gap by providing the first detailed analysis of the overall impact of combined in-service deterioration features on the overall thermal performance of HP NGVs. It is hoped that the results from this paper will be a useful step toward whole-life engine performance modeling and assessment.

Acknowledgment

The financial support of Rolls-Royce plc and the Aerospace Technology Institute is gratefully acknowledged. Technical discussions with James Cartledge regarding Appendix D are also gratefully acknowledged.

Conflict of Interest

There are no conflicts of interest.

Data Availability Statement

The authors attest that all data for this study are included in the paper.

Nomenclature

- c = recovery ratio, -
- \bar{h} = heat transfer coefficient, $\text{W m}^{-2} \text{K}^{-1}$
- \bar{h} = area-averaged heat transfer coefficient, $\text{W m}^{-2} \text{K}^{-1}$
- l = streamwise surface length, m
- \dot{m} = mass flowrate, kg s^{-1}
- p = static pressure, Pa
- r = recovery factor, -
- t = thickness, m
- B = blowing ratio, -
- C = tangential chord, m
- D = diameter of film cooling hole, m
- I = momentum flux ratio, -
- L = streamwise surface length fraction, -

M = Mach number, –
 S = span fraction, –
 T = temperature, K
 k_s = equivalent sandgrain roughness height, m
 p_0 = total pressure, Pa
 q_{cam} = total radiance measured by IR camera, $W m^{-2} sr^{-1}$
 q_{opt} = emitted ZnSe window radiance, $W m^{-2} sr^{-1}$
 q_w = emitted vane external wall radiance, $W m^{-2} sr^{-1}$
 q'_w = transmitted vane external wall radiance, $W m^{-2} sr^{-1}$
 q_s = emitted surrounding surface radiance, $W m^{-2} sr^{-1}$
 q'_s = reflected radiance from surrounding surfaces, $W m^{-2} sr^{-1}$
 q''_s = reflected and transmitted radiance from surrounding surfaces, $W m^{-2} sr^{-1}$
 q^* = total surrounding radiance ($q'_s + q_{opt}$), $W m^{-2} sr^{-1}$
 C_{ax} = axial chord, m
 R_a = centerline average roughness height, m
 T_0 = total temperature, K
 $T_{0,mixed}$ = total temperature of mixing layer, K
 T_{bb} = equivalent black-body temperature, K
 T_{opt} = ZnSe window temperature, K
 T_s = temperature of surrounding surfaces, K
 T_w = evaluated vane external surface temperature, K
 Pr = Prandtl number, –
 Tu = inlet turbulence intensity, –
 Re_C = exit Reynolds number based on tangential chord, –

Greek Symbols

β = bias uncertainty, –
 γ = ratio of specific heat capacities, –
 Γ = capacity, $kg s^{-1} K^{1/2} Pa^{-1}$
 ε = emissivity, –
 η_f = adiabatic film cooling effectiveness, –
 $\bar{\eta}_f$ = laterally average adiabatic film cooling effectiveness, –
 $(\bar{\eta}_f)$ = area-average adiabatic film cooling effectiveness, –
 θ_{bb} = black-body effectiveness, –
 $\bar{\theta}_w$ = overall cooling effectiveness, –
 $\bar{\theta}_w$ = area-average overall cooling effectiveness, –
 $\Delta\bar{\theta}_w$ = change in area-average overall cooling effectiveness, –
 κ = thermal conductivity, $W m^{-1} K^{-1}$
 σ = Stefan-Boltzmann constant, –
 τ = transmissivity, –

Subscripts

1 = upstream of HP NGVs
2 = downstream of HP NGVs
as = as-sprayed
ax = axial
bb = black body
c = coolant
cam = camera
det = deteriorated
he = heat-exposed
is = isentropic
opt = optic
p = paint
ref = reference
s = surrounding

Appendix A: One-Dimensional Heat Transfer Model

In this section, we introduce the steady one-dimensional heat transfer model and the associated nominal boundary conditions used to decouple the effect of individual deterioration features. A schematic of the model is shown in Fig. 6. It consists of a two-layer vane wall (metal and TBC) subjected to a hot external flow with heat transfer coefficient h and an internal coolant flow at

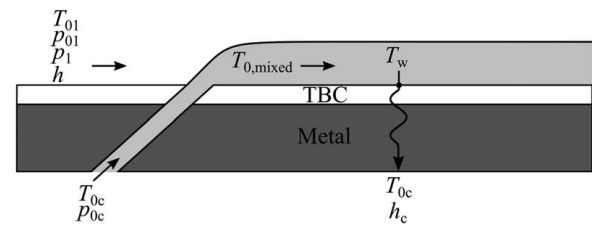


Fig. 6 Schematic of the heat transfer model (not to scale)

temperature T_{0c} with heat transfer coefficient h_c . The external surface has a mixing film cooling layer, which entrains mainstream gas at temperature T_{01} , and which is described by an adiabatic film cooling effectiveness, η_f . This gives us the total temperature of the mixing layer

$$T_{0,mixed} = T_{01} - \eta_f(T_{01} - T_{0c}) \quad (A1)$$

The temperature of the mixing layer ($T_{0,mixed}$) is the external driving temperature. Heat conduction is one dimension in the through-wall direction.

The nominal temperatures T_{01} and T_{0c} are those of a typical run and are listed in Table 3. The model was run for boundary conditions typical of the pressure side ($-80 < L < 0\%$) and late suction side ($40 < L < 100\%$). Nominal external HTC (h_{ps} and h_{ss}) and adiabatic film cooling effectiveness values ($\eta_{f,ps}$ and $\eta_{f,ss}$) for each region are average values (over the entire region) obtained from the open literature. These are listed in Table 7 with the original source for the values. Wall thermal properties and physical parameters are also listed. The nominal thermal conductivity of the TBC ($\kappa_{TBC,as}$) is representative of its as-sprayed condition [30] and the thermal conductivity of the metal is typical of a nickel-based superalloy (commonly used in turbine components) [45]. Values for internal HTCs ($h_{c,ps}$ and $h_{c,ss}$) were taken to be those that reconcile the output of the one-dimensional thermal model with measured average values of overall cooling effectiveness on the vane. This ensures accuracy of the decoupling process.

Appendix B: Emissivity of Deteriorated Thermal Barrier Coating

There are numerous papers which consider the emissivity of as-sprayed (new) and heat-exposed (but otherwise not deteriorated) TBC [36–39], but there is a lack of data regarding the emissivity of deteriorated TBC subject to significant oxidation and deposition (and associated discoloration). To the authors' knowledge, the only open-literature study is that of Liebert [36], who found no change in emissivity of the TBC of a turbine component after 150 h of engine operation: this is a relatively short operating time compared to the engine-run vanes in the present study. A method

Table 7 Boundary conditions and constants used in the one-dimensional heat transfer model

Property	Value	Source
h_{ps}	$625 W m^{-2} K^{-1}$	[46]
h_{ss}	$900 W m^{-2} K^{-1}$	[46]
$h_{c,ps}$	$2000 W m^{-2} K^{-1}$	–
$h_{c,ss}$	$2500 W m^{-2} K^{-1}$	–
$\eta_{f,ps}$	0.25	[47]
$\eta_{f,ss}$	0.20	[47]
t_{TBC}	0.15 mm	–
κ_{TBC}	$1.34 W m^{-1} K^{-1}$	[30]
t_{metal}	1.50 mm	–
κ_{metal}	$8.00 W m^{-1} K^{-1}$	[45]

was therefore developed to provide an estimate of the emissivity of the deteriorated TBC of the vanes in the present study. The method was validated by application to heat-exposed but otherwise non-deteriorated TBC, for which the emissivity is independently known.

A photograph of the calibration system and corresponding IR image are shown in Fig. 7 (frames a and b, respectively), applied to the heat-exposed but otherwise non-deteriorated TBC reference surface. An identical system was used on the deteriorated TBC to be calibrated. The IR image was captured during a run (situation with high through-wall heat flux) and presented in terms of black-body effectiveness defined by

$$\theta_{bb} = \frac{T_{01} - T_{bb}}{T_{01} - T_{oc}} \quad (B1)$$

The calibration system comprises: an isothermal calibration patch, marked A, which is of known uniform temperature (thermocouple) and known emissivity (overpainted with matt black paint); a proximate matt black paint patch, marked B, of known emissivity but unknown temperature; and a surrounding surface region (C or D, for the two example cases) for which the surface effectiveness is to be evaluated. Further discussion around the necessity for an isothermal calibration patch can be found in Ref. [34].

Examining Fig. 7(b), we see no visible difference between θ_{bb} on the paint patch, B, and surrounding surface, C. The maximum difference in θ_{bb} between the paint patch and the surrounding surface was measured to be 0.2%. This was true also for the case of the deteriorated TBC to be calibrated. That is—in both cases—the equivalent black-body temperature (T_{bb}) of the paint patch and proximate TBC surface were essentially the same. We now compute the maximum difference in surface emissivity (between B and C) that is possible under the condition $T_{bb,B} = T_{bb,C}$.

For $T_{bb,B} = T_{bb,C}$, it is possible to show (Eq. (3)) that the effectiveness values at B and C (ε_B and ε_C , respectively) must be related by

$$\frac{\varepsilon_B}{\varepsilon_C} = \frac{T_{w,C}^4 - T_s^4}{T_{w,B}^4 - T_s^4} \quad (B2)$$

in which T_s is the equivalent temperature of the surrounding surfaces, which can be found by applying Eq. (3) to the isothermal calibration patch A, for which both surface temperature ($T_{w,A}$) and emissivity (ε_A) are known (see Ref. [34]). The temperature of the ZnSe window (T_{opt}) is known by measurement. Evaluating T_s in this way we get

$$T_s = \sqrt[4]{\frac{T_{bb,A}^4 - \tau_{opt}\varepsilon_A T_{w,A}^4 - (1 - \tau_{opt})T_{opt}^4}{\tau_{opt}(1 - \varepsilon_A)}} \quad (B3)$$

We now calculate the relationship between $T_{w,B}$ and $T_{w,C}$ using a

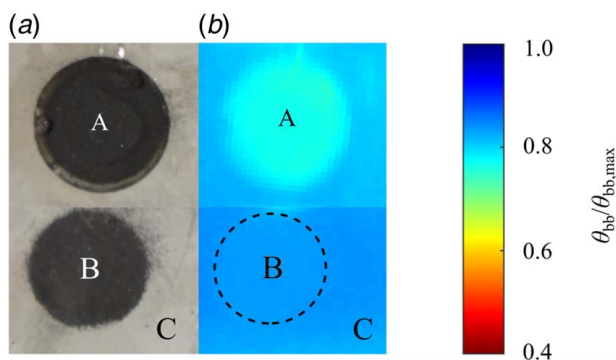


Fig. 7 (a) Photograph of calibration system on surface with heat-exposed but otherwise nondeteriorated TBC and (b) black-body effectiveness map of same under conditions of high through-wall heat flux

simple 1D heat transfer model. Taking local estimates for quasi-steady-state through-wall heat flux, and noting the thermal resistance of the additional paint layer (10 μm thick; $\kappa_p = 1.00 \text{ W m}^{-1} \text{ K}^{-1}$ [48]), it is possible to show using a 1D heat transfer model that for identical values of T_{bb} (i.e., $T_{bb,B} = T_{bb,C}$) the external surface temperature $T_{w,B}$ is higher than $T_{w,C}$ by approximately 0.04%, that is $T_{w,B} \cong T_{w,C} \times 1.0004$. The small temperature increase is caused by the additional thermal resistance of the paint layer in the presence of the estimated through-wall heat flux.

Combining Eqs. (B3) and (B2), for the condition $T_{w,B} \cong T_{w,C} \times 1.0004$, we get $\varepsilon_B \cong \varepsilon_C \times 1.002$. That is, when indistinguishable equivalent black-body temperatures are measured on the paint patch (B) and the surrounding surface (C), the implication (in our system) is that the emissivities are the same to within 0.2%. As this condition ($T_{bb,B} = T_{bb,C}$) was met for both the heat-exposed but otherwise non-deteriorated TBC reference surface, and for the deteriorated TBC to be calibrated, we conclude that in both instances the emissivities are effectively the same as that of matt black paint, i.e., $\varepsilon_B = \varepsilon_C = 0.98$.

Appendix C: Bias Uncertainty Analysis

The bias uncertainty in measured and derived quantities is now considered.

The mainstream flow total temperature (T_{01}) was measured by 32 K-type thermocouples each with a quoted bias uncertainty of $\pm 1.1 \text{ K}$ (special limits of error, SLE), or $\pm 0.31\%$ (350 K nominal). The bias uncertainty in measured temperature (average of 32 measurements) was therefore estimated to be $\beta_{T_{01}}^{\%} = \pm 0.31/\sqrt{32} \% = \pm 0.06\%$ to 95% confidence (see Table 8). The coolant flow total temperature (T_{oc}) was measured using 8 K-type thermocouples each with a quoted bias uncertainty of $\pm 1.1 \text{ K}$ (SLE), or $\pm 0.38\%$ (290 K nominal). The bias uncertainty in the mean of all the eight measurements was therefore estimated to be $\beta_{T_{oc}}^{\%} = \pm 0.38/\sqrt{8} \% = \pm 0.13\%$ to 95% confidence.

The equivalent black-body surface temperature (T_{bb}) was measured by an IR camera calibrated in-situ against a calibration system with a single K-type thermocouple. The error in T_{bb} is therefore dominated by the thermocouple uncertainty, which was estimated as $\pm 1.1 \text{ K}$ (SLE), or $\pm 0.35\%$ (310 K nominal). The processing method is such that at the location of the calibration patch T_{bb} is real-time-normalized to the value measured by the calibration thermocouple. Thus, we take the uncertainty in T_{bb} at the location of the calibration patch to be $\pm 0.35\%$ (310 K nominal). At other locations on the vane surface, where the surface temperature is different than that at the calibration system, an additional uncertainty is introduced due to errors in linearity, hysteresis, and repeatability (LHR) of the IR camera black-body calibration. This is estimated by the IR camera manufacturer to be $\pm 0.05\%$ of the measured T_{bb} [49]. The worst-case bias uncertainty in T_{bb} is therefore estimated to be $\beta_{T_{bb}}^{\%} = \pm 0.40\%$ to 95% confidence.

Table 8 Summary of bias uncertainty (to 95% confidence) in directly measured and derived quantities

Quantity	$\beta^{\%}$	Nominal value
T_{01}	$\pm 0.06\%$	350 K
T_{oc}	$\pm 0.13\%$	290 K
T_{bb}	$\pm 0.40\%$	310 K
τ_{opt}	$\pm 3.00\%$	0.95
$\varepsilon_{TBC,as}$	$\pm 1.02\%$	0.98
$\varepsilon_{TBC,he}$	$\pm 1.02\%$	0.98
$\varepsilon_{TBC,det}$	$\pm 1.02\%$	0.98
T_w	$\pm 0.51\%$	310 K
θ_w	$\pm 2.83\%$	0.70
$\bar{\theta}_w$	$\pm 2.83\%$	0.70
$\Delta\bar{\theta}_w$	$\pm 3.73\%$	0.70

The bias uncertainty in the transmissivity of the ZnSe window (τ_{opt}) is quoted to $\pm 3.00\%$ by the window manufacturer. The uncertainty in the emissivity of as-sprayed TBC ($\varepsilon_{\text{TBC,as}}$) and heat-exposed but otherwise not deteriorated TBC ($\varepsilon_{\text{TBC,he}}$) is not reported in the open literature, but a survey of the reported emissivities from three papers [36,37,39] shows that the emissivity is typically in the range $0.97 < \varepsilon_{\text{TBC,as/he}} < 0.99$ and we therefore take the uncertainty in $\varepsilon_{\text{TBC,as/he}}$ to be ± 0.01 or $\pm 1.02\%$ with a nominal value of 0.98. We have demonstrated (Appendix B) that the observed difference in emissivity between deteriorated TBC and non-deteriorated TBC was negligible, and we therefore take the uncertainty $\varepsilon_{\text{TBC,det}}$ to be the same as $\varepsilon_{\text{TBC,as}}$ and $\varepsilon_{\text{TBC,he}}$. These values are summarized in Table 8.

Performing a Monte Carlo simulation with the uncertainties in the directly measured quantities listed in Table 8 as inputs, we estimate the bias uncertainty in evaluated external wall temperature (T_w) to be $\pm 0.51\%$. Although we are primarily interested in the change in area-averaged overall cooling effectiveness, $\bar{\Delta\theta}_w$ (defined as the difference in $\bar{\theta}_w$ between a new reference vane and a deteriorated vane), we also perform crude estimates of the absolute errors in local and area-averaged overall cooling effectiveness values θ_w and $\bar{\theta}_w$ arising from errors in T_w and M (from CFD, and affecting c_m and c_c). Estimating the error (difference between CFD and experiment) in the local value M to be 2.00%, this gives errors in the absolute values θ_w and $\bar{\theta}_w$ of 2.83% (based on nominal values of 0.70). So far as interpreting the normalized data of Fig. 4 is concerned, the error in the change in area-averaged overall cooling effectiveness, $\bar{\Delta\theta}_w$, is more important. Here we can assume that spatial distributions of c_m and c_c are essentially the same for all vanes. Additionally, the uncertainties in T_{01} , T_{0c} , τ_{opt} and ε (used to calculate the uncertainty in T_w) are relatively highly correlated between vanes (same instrumentation and material property uncertainties). Taking a worst-case assumption that all errors are uncorrelated, however, we obtain an upper-bound estimate of the uncertainty in $\bar{\Delta\theta}_w$ as $\pm 3.73\%$ of the nominal value of $\bar{\theta}_w$. This is dominated by uncertainty in T_{bb} .

Appendix D: Definition of Overall Cooling Effectiveness

A common definition of overall cooling effectiveness θ_w is

$$\theta_w = \frac{c_m T_{01} - T_w}{c_m T_{01} - T_{0c}} \quad (\text{D1})$$

where the local recovery ratio c_m is used to account for compressibility effects associated with the mainstream gas at the vane external Mach number, but we do not account for similar effects associated with the coolant stream. This—we could argue—on the basis that the mainstream flow, being confined exclusively to the external compressible flow field, is unavoidably subject to a reduction in temperature due to recovery effects in the near-wall region. This definition suffers from the obvious problem that it is not necessarily limited to the range $0 \leq \theta_w \leq 1$. Indeed, for a perfectly effective cooling system (i.e., infinite coolant flow, infinite internal HTC and adiabatic film effectiveness at unity), the theoretical lowest temperature in the system is $c_c T_{0c}$, where the local recovery ratio c_c is that associated with the vane external Mach number and the coolant gas temperature is that at inlet to the vane. In the limit $T_w \rightarrow c_c T_{0c}$, it is clear that $\theta_w > 1$ is possible in the definition of Eq. (D1). A remedy is to additionally include a local recovery ratio term for the coolant stream temperature, giving

$$\theta_w = \frac{c_m T_{01} - T_w}{c_m T_{01} - c_c T_{0c}} \quad (\text{D2})$$

This has the advantage of limiting the theoretical range of θ_w to between zero and unity (i.e., $0 \leq \theta_w \leq 1$) for the situation of combined internal and film cooling. This is the form we use in the

present paper. We justify it on the basis that the coolant flow is also subject to the external compressible flow field on the external surface of the vane (in the mixing layer).

References

- [1] Ozgurluk, Y., Doleker, K. M., Ahlatci, H., and Karaoglanli, A. C., 2018, "Investigation of Hot Corrosion Behavior of Thermal Barrier Coating (TBC) Systems With Rare Earth Contents," *Arab. J. Geosci.*, **11**(11), p. 267.
- [2] Prenter, R., Ameri, A., and Bons, J. P., 2016, "Deposition on a Cooled Nozzle Guide Vane With Nonuniform Inlet Temperatures," *ASME J. Turbomach.*, **138**(10), p. 101005.
- [3] Gell, M., Eric, J., Krishnakumar, V., McCarron, K., Barber, B., Sohn, Y.-H., and Tolpygo, V. K., 1993, "Bond Strength, Bond Stress and Spallation Mechanisms of Thermal Barrier Coatings," *Surf. Coat. Technol.*, **120–121**, pp. 53–60.
- [4] Hamed, A. A., Tabakoff, W., Rivir, R. B., Das, K., and Arora, P., 2005, "Turbine Blade Surface Deterioration by Erosion," *ASME J. Turbomach.*, **127**(3), pp. 445–452.
- [5] Kurz, R., and Brun, K., 2001, "Degradation in Gas Turbine Systems," *ASME J. Eng. Gas Turbines Power*, **123**(1), pp. 70–77.
- [6] Bons, J. P., 2010, "A Review of Surface Roughness Effects in Gas Turbines," *ASME J. Turbomach.*, **132**(2), p. 021004.
- [7] Darolia, R., 2013, "Thermal Barrier Coatings Technology: Critical Review, Progress Update, Remaining Challenges and Prospects," *Int. Mater. Rev.*, **58**(6), pp. 315–348.
- [8] Bogard, D. G., Schmidt, D. L., and Tabbita, M., 1998, "Characterization and Laboratory Simulation of Turbine Airfoil Surface Roughness and Associated Heat Transfer," *ASME J. Turbomach.*, **120**(2), pp. 337–342.
- [9] Kirolos, B., and Povey, T., 2014, "Reverse-Pass Cooling Systems for Improved Performance," *ASME J. Turbomach.*, **136**(11), p. 111004.
- [10] Kirolos, B., and Povey, T., 2016, "Cooling Optimization Theory—Part I: Optimum Wall Temperature, Coolant Exit Temperature, and the Effect of Wall/Film Properties on Performance," *ASME J. Turbomach.*, **138**(8), p. 081002.
- [11] Kirolos, B., and Povey, T., 2016, "Cooling Optimization Theory—Part II: Optimum Internal Heat Transfer Coefficient Distribution," *ASME J. Turbomach.*, **138**(8), p. 081003.
- [12] Turner, A. B., Tarada, F. H. A., and Bayley, F. J., 1985, "Effects of Surface Roughness on Heat Transfer to Gas Turbine Blades," *AGARD Heat Transfer and Cool. Gas Turbines*, **9**, pp. 1–10.
- [13] Bunker, R. S., 1997, "Separate and Combined Effects of Surface Roughness and Turbulence Intensity on Vane Heat Transfer," Proceedings of the ASME 1997 International Gas Turbine and Aeroengine Congress and Exhibition, Orlando, FL, Paper No. 97-GT-135.
- [14] Stripf, M., Schulz, A., and Wittig, S., 2005, "Surface Roughness Effects on External Heat Transfer of a HP Turbine Vane," *ASME J. Turbomach.*, **127**(1), pp. 200–208.
- [15] Lorenz, M., Schulz, A., and Bauer, H., 2012, "Experimental Study of Surface Roughness Effects on a Turbine Airfoil in a Linear Cascade—Part I: External Heat Transfer," *ASME J. Turbomach.*, **134**(4), p. 041006.
- [16] Blair, M. F., 1994, "An Experimental Study Heat Transfer in a Large-Scale Turbine Rotor Passage," *ASME J. Turbomach.*, **116**(1), pp. 1–13.
- [17] Rutledge, J. L., Robertson, D., and Bogard, D. G., 2006, "Degradation of Film Cooling Performance on a Turbine Vane Suction Side Due to Surface Roughness," *ASME J. Turbomach.*, **128**(3), pp. 547–554.
- [18] Abuaf, N., Bunker, R. S., and Lee, C. P., 1998, "Effects of Surface Roughness on Heat Transfer and Aerodynamic Performance of Turbine Airfoils," *ASME J. Turbomach.*, **120**(3), pp. 522–529.
- [19] Hoff, A., Drost, U., and Böls, A., 1996, "Heat Transfer Measurements on a Turbine Airfoil at Various Reynolds Numbers and Turbulence Intensities Including Effects of Surface Roughness," Proceedings of the ASME 1996 International Gas Turbine and Aeroengine Congress and Exhibition, Birmingham, UK, Paper No. 96-GT-169.
- [20] Boyle, R. J., and Senyitko, R. G., "Effects of Surface Roughness on Turbine Vane Heat Transfer," Proceedings of the ASME Turbo Expo 2005, Reno, NV, Paper No. GT2005-69133.
- [21] Bacci, T., Picchi, A., Lenzi, T., Facchini, B., and Innocenti, L., 2021, "Effect of Surface Roughness and Inlet Turbulence Intensity on a Turbine Nozzle Guide Vane External Heat Transfer: Experimental Investigation on a Literature Test Case," *ASME J. Turbomach.*, **143**(4), p. 041006.
- [22] Erickson, E. L., Ames, F. E., and Bons, J. P., 2012, "Effects of a Realistically Rough Surface on Vane Heat Transfer Including the Influence of Turbulence Condition and Reynolds Number," *ASME J. Turbomach.*, **134**(2), p. 021013.
- [23] Michaud, M., Jackson, D., Goenaga, F., and Povey, T., 2022, "Experimental Study of Impact of In-Service Deterioration on Aerodynamic Performance of High-Pressure Nozzle Guide Vanes," under review.
- [24] Barlow, D. N., and Kim, Y. W., 1995, "Effect of Surface Roughness on Local Heat Transfer and Film Cooling Effectiveness," Proceedings of the ASME 1995 International Gas Turbine and Aeroengine Congress and Exposition, Houston, TX, USA, Paper No. 95-GT-014.
- [25] Lawson, S. A., and Thole, K. A., 2011, "Effects of Simulated Particle Deposition on Film Cooling," *ASME J. Turbomach.*, **133**(2), p. 021009.
- [26] Goldstein, R. J., Eckert, E. R. G., Chiang, H. D., and Elovic, E., 1985, "Effect of Surface Roughness on Film Cooling Performance," *ASME J. Eng. Gas Turbines Power*, **107**(1), pp. 111–116.
- [27] Schmidt, D. L., and Bogard, D. G., 1996, "Effects of Free-Stream Turbulence and Surface Roughness on Film Cooling," Proceedings of the ASME 1996

- International Gas Turbine and Aeroengine Congress and Exhibition, Birmingham, UK, Paper No. 96-GT-462.
- [28] Schmidt, D. L., Sen, B., and Bogard, D. G., 1996, "Effects of Surface Roughness on Film Cooling," Proceedings of the ASME 1996 International Gas Turbine and Aeroengine Congress and Exhibition, Birmingham, UK, Paper No. 96-GT-299.
- [29] Bogard, D. G., Snook, D., and Kohli, A., 2003, "Rough Surface Effects on Film Cooling of the Suction Side Surface of a Turbine Vane," Proceedings of the ASME 2003 International Mechanical Engineering Congress and Exposition, Washington, DC, Paper No. IMECE2003-42061.
- [30] Rätzer-Scheibe, H.-J., and Schulz, U., 2007, "The Effects of Heat Treatment and Gas Atmosphere on the Thermal Conductivity of APS and EB-PVD PYSZ Thermal Barrier Coatings," *Surf. Coat. Technol.*, **201**(18), pp. 7880–7888.
- [31] Wellman, R. G., and Nicholls, J. R., 2007, "A Review of the Erosion of Thermal Barrier Coatings," *J. Phys. D: Appl. Phys.*, **40**(16), pp. 293–305.
- [32] Kirolos, B., Lubbock, R., Beard, P., Goenaga, F., Rawlinson, A., Janke, E., and Povey, T., 2017, "ECAT: An Engine Component Aerothermal Facility at the University of Oxford," Proceedings of the ASME Turbo Expo 2017, Charlotte, NC, Paper No. GT2017-64736.
- [33] Bons, J., 2005, "A Critical Assessment of Reynolds Analogy for Turbine Flows," *ASME J. Heat Transfer-Trans. ASME*, **127**(5), pp. 472–485.
- [34] Michaud, M., Ormano, F., Chowdhury, N. H. K., and Povey, T., 2020, "Methodology for High-Accuracy Infrared Calibration in Environments With Through-Wall Heat Flux," *J. Glob. Power Propuls. Soc.*, **4**, pp. 1–13.
- [35] Kirolos, B., and Povey, T., 2017, "Laboratory Infrared Thermal Assessment of Laser-Sintered High-Pressure Nozzle Guide Vanes to Derisk Engine Design Programs," *ASME J. Turbomach.*, **139**(4), p. 041009.
- [36] Liebert, C. H., 1978, "Emittance and Absorbance of NASA Ceramic Thermal Barrier Coating System," NASA Technical Paper 1190.
- [37] González-Fernández, L., del Campo, L., Pérez-Sáez, R. B., and Tello, M. J., 2012, "Normal Spectral Emittance of Inconel 718 Aeronautical Alloy Coated With Yttria Stabilized Zirconia Films," *J. Alloys Compd.*, **513**, pp. 101–106.
- [38] FLIR, 2018, *FLIR Product Catalog 2018*, FLIR System, Inc., Wilsonville, OR, Publication No. T559480.
- [39] Manara, J., Arduini-Schuster, M., Rätzer-Scheibe, H.-J., and Schulz, U., 2009, "Infrared-Optical Properties and Heat Transfer Coefficients of Semitransparent Barrier Coatings," *Surf. Coat. Technol.*, **203**(8), pp. 1059–1068.
- [40] Keller, B. P., Nelson, S. E., Walton, K. L., Ghosh, T. K., Tompson, R. V., and Loyalka, S. K., 2015, "Total Hemispherical Emissivity of Inconel 718," *Nucl. Eng. Des.*, **287**, pp. 11–18.
- [41] Greene, G. A., Finfrock, C. C., and Irvine, T. F., 2000, "Total Hemispherical Emissivity of Oxidized Inconel 718 in the Temperature Range 300–1000 °C," *Exp. Therm. Fluid. Sci.*, **22**(3–4), pp. 145–153.
- [42] Del Campo, L., Pérez-Sáez, R. B., González-Fernández, L., Esquisabel, X., Fernández, I., González-Martín, P., and Tello, M. J., 2010, "Emissivity Measurements on Aeronautical Alloys," *J. Alloys Compd.*, **489**(2), pp. 482–487.
- [43] Burdett, D., Goenaga, F., and Povey, T., 2021, "Understanding Capacity Sensitivity of Cooled Transonic Nozzle Guide Vanes: A Parametric Experimental and Computational Study of the Impact of Trailing Edge Geometry," *ASME J. Turbomach.*, **143**(5), p. 051001.
- [44] Eckert, E. R. G., and Drake, R. M., 1972, *Analysis of Heat and Mass Transfer*, McGraw-Hill, New York.
- [45] Wee, S., Do, J., Kim, K., Lee, C., Seok, C., Choi, B.-G., Choi, Y., and Kim, W., 2020, "Review on Mechanical Thermal Properties of Superalloys and Thermal Barrier Coating Used in Gas Turbines," *Appl. Sci.*, **10**(16), p. 5476.
- [46] Qureshi, I., Smith, A. D., and Povey, T., 2013, "HP Vane Aerodynamics and Heat Transfer in the Presence of Aggressive Inlet Swirl," *ASME J. Turbomach.*, **135**(2), p. 021040.
- [47] Ames, F. E., 1998, "Aspects of Vane Film Cooling With High Turbulence: Part II—Adiabatic Effectiveness," *ASME J. Turbomach.*, **120**(4), pp. 777–784.
- [48] Raghu, O., and Philip, J., 2006, "Thermal Properties of Paint Coatings on Different Backings Using a Scanning Photo Acoustic Technique," *Meas. Sci. Technol.*, **17**(11), pp. 2945–2949.
- [49] Parker, J., and Povey, T., 2022, "Method for Determining Adiabatic Film Effectiveness in Presence of Thermal Boundary Layer," *ASME J. Turbomach.*, **144**(5), p. 051010.